Determining Plasmonic Hot Electrons and Photothermal Effects during H_2 Evolution with TiN–Pt Nanohybrids

Sourav Rej, Luca Mascaretti, Eva Yazmin Santiago, Ondřej Tomanec, Štěpán Kment, Zhiming Wang, Radek Zbořil, Paolo Fornasiero, Alexander O. Govorov,* and Alberto Naldoni*

ABSTRACT: Hydrogen storage in chemical compounds is a promising strategy to enable lightweight, high-density, and safe hydrogen technologies. However, the hydrogen release rate from these chemicals is limited by the intrinsic catalytic activity of metal catalysts, which can be enhanced by light irradiation. Here, nanohybrids including a core of plasmonic TiN and multiple Pt nanocrystal catalytic centers are assembled and show, under resonant conditions at 700 nm, hot electron-driven hydrogen evolution from ammonia borane at an apparent quantum yield of 120%. It is also demonstrated that solar irradiation enhances the activity of TiN–Pt nanohybrids by one order of magnitude through two synergistic mechanisms: hot electrons and collective-heating contributions. Using the microscopic calculation of the photo-induced temperature around a single nanocrystal, it is revealed that the collective plasmonic heating regime dominates the macroscopic temperature distribution in the system. The presented data show that plasmonic hot electrons and photothermal heating can be used in synergy to trigger hydrogen release from ammonia borane on demand, providing a general strategy for greatly enhancing the activity of metal catalysts in the dark.

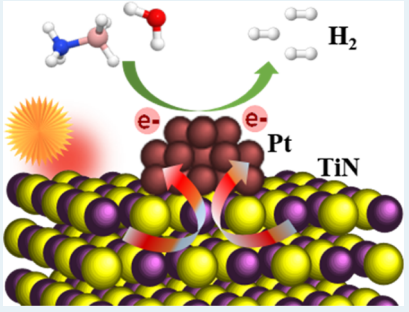

KEYWORDS: *plasmonics, titanium nitride, ammonia-borane, hydrogen evolution, photocatalysis*

INTRODUCTION

The development of lightweight storage systems for on-board storage and controlled release of hydrogen (H_2) is a limiting factor for the widespread utilization of energy technologies based on fuel cells.[1−3] Transport and storage of H_2 as a gas or liquid in highly pressurized tanks may not provide the required fuel density for long transportation, while increasing hazard concerns. Thus, there is a continued interest in finding alternative means to store H_2 in the high-density form, from which it can be released on demand at viable rates and temperatures (below 70 °C).[1]

Some examples of recently investigated materials for H_2 storage include metal hydrides and porous sorbent materials.[2,4] In addition to these, a promising class of compounds is chemical complexes wherein the H_2 is stored in X–H bonds (X = C, B, N, or O). In this case, H_2 can be released thermally or through the aid of a catalyst.[4] Ammonia borane (NH_3BH_3) is a particularly appealing candidate material owing to its high gravimetric H_2 capacity (19.6 wt %), low molecular weight (30.7 g mol^{-1}), and high stability in solution, while being nonflammable and nonexplosive under standard conditions.[3] The dehydrogenation of NH_3BH_3 is a downhill reaction that potentially results in three equivalents of H_2

$$NH_3BH_3 + 4H_2O \rightarrow NH_4^+B(OH)_4^- + 3H_2\uparrow \quad (1)$$

A typical approach to H_2 evolution from NH_3BH_3 is the use of catalytic metals, which allows appreciable rates in dark conditions.[5] Supported Pt-,[6−10] Rh-,[11] and Ru[5]-based nanocatalysts usually showed higher H_2 production rates. However, the use of these catalytic metals poses relevant issues in terms of cost and scalability of H_2 storage technologies. Recently, the use of plasmonic materials (noble metals and metal oxides) has emerged as a general strategy to enhance the activity of catalytic metals for NH_3BH_3 dehydrogenation by light irradiation.[12−16]

Upon light illumination, plasmonic photocatalysts support the collective oscillations of free carriers, that is, localized surface plasmon resonance (LSPR), which concentrates light at the nanoscale and produce very intense electric fields.[17−19] Surface plasmons may then undergo nonradiative decay, generating highly energetic electron–hole pairs (hot carriers), which have shown the capability to drive chemical reactions[20−23] with product selectivity,[24−26] as well as the ability to catalyze multielectron processes like CO_2 reduction.[27−31]

The temperature of hot carriers eventually cool down via electron–electron and electron–phonon scattering within 100

ps, causing an increase in the lattice temperature that results in the heating of the plasmonic material.[32−34] This thermal energy can enhance the reaction rate with an Arrhenius-like dependence, and it has been the focus of recent efforts devoted to distinguishing the photothermal contribution from the plasmonic hot electron effects.[35−37]

Here, we show that refractory, acid-resistant, fuel cell-compatible plasmonic nanohybrids including plasmonic TiN[38−42] nanocubes decorated with Pt nanocrystals efficiently drive H_2 evolution from ammonia borane dehydrogenation with apparent quantum yield (AQY) exceeding 100% under monochromatic light at 700 nm (incident intensity: 2 mW cm^{-2}). Under solar irradiation, the activity of TiN−Pt nanohybrids is enhanced by one order of magnitude (from 32 to 346 mol_{H_2} mol_{Pt}^{-1} min^{-1}) through the synergistic effect of plasmonic hot electrons and heating. We demonstrate that at high solar intensity, H_2 evolution is both an electron- and thermally driven process, in which hot electrons are mainly generated in TiN and then transferred to the Pt surface, thus decreasing the energetic requirement to access the transition state (TS) of the rate-determining step, that is, water cleavage.

EXPERIMENTAL SECTION

Synthesis of TiN−Pt Nanohybrids. Before depositing Pt nanocrystals, commercial TiN nanocubes (PlasmaChem GmbH, ∼50 nm average size) were treated with concentrated HCl to clean the TiN surface according to the following procedure: 20 mL of concentrated HCl (35%, Penta) and 400 mg of TiN nanocubes were sonicated for 10 min at room temperature (RT) under sealed conditions. After that, the reaction mixture was kept at 65 °C on a preheated water bath for 1 h under a continuous nitrogen flow. Upon completion of the reaction, the TiN nanocubes were then washed once with 40 mL of water/ethanol (1:1 volume ratio) mixture and further twice with 40 mL of anhydrous ethanol. TiN nanocubes were then concentrated in 5 mL of anhydrous ethanol and dried in an oven at 80 °C overnight.

The dried TiN nanocubes were crushed into a fine powder using a spatula prior to Pt nanocrystal deposition. First, 92 mg of acid-treated TiN nanocubes were suspended in 50 mL of deionized water (DI-H_2O) and sonicated for 20 min. An appropriate amount of K_2PtCl_4 (Sigma-Aldrich) were dissolved in DI-H_2O and added dropwise to the aforementioned solution of TiN nanocubes under vigorous stirring; afterward, the resulting solution was stirred for additional 2 h. Subsequently, 1 mL of 3 M aqueous solution NaOH (Alfa Aesar) was added dropwise to adjust the solution pH at ∼13, followed by stirring for 1 h. Formaldehyde (1 mL) (37%, Penta) was then added dropwise to the solution with vigorous stirring, and the reaction mixture was placed in a preheated water bath at 85 °C for 1.5 h under a continuous nitrogen flow. The TiN−Pt nanohybrids were washed using the same procedure as above. After washing, all nanohybrids were then concentrated in 50 mL of DI-H_2O. An aqueous HCl solution (1.8 mL) (10% vol) were added dropwise to the nanocrystal solution and continuously stirred at 700 rpm overnight. TiN−Pt nanohybrids were further washed and collected using the same washing procedure described in the previous section. The as-synthesized TiN−Pt nanohybrids were concentrated in 5 mL of anhydrous ethanol and dried in an oven at 80 °C for overnight. The so-obtained fine powder was reduced in a furnace under a H_2/N_2 flow (10%:90% vol, 200 sccm) for 2 h at 200 °C. The reduced TiN−Pt nanohybrids were kept in closed glass vials under an argon atmosphere before and after their use. Inductively coupled plasma mass spectrometry (ICP−MS) analysis confirmed that the Pt loading was 8 wt %. In order to perform control experiments, a Pt/Al_2O_3 catalyst was prepared. Pt nanocrystals were synthesized by reducing K_2PtCl_4 in the presence of NaOH (pH > 12) at 145 °C for 3 h in ethylene glycol. Then, this colloidal solution was vigorously mixed with Al_2O_3 followed by washing and overnight drying at 80 °C. The so-obtained Pt/Al_2O_3 catalyst was reduced at 100 °C for 1 h under H_2 flow before usage.

Characterization. Powder X-ray diffraction patterns of the material were determined using an X'Pert PRO MPD diffractometer (PANalytical) with iron-filtered Co Kα radiation (40 kV, 30 mA, λ = 0.1789 nm). X-ray photoelectron spectroscopy (XPS) analysis were performed on a PHI 5000 VersaProbe II XPS system (Physical Electronics) with a monochromatized Al Kα source (15 kV, 50 W) and a photon energy of 1486.7 eV. High-resolution spectra were scaled using the adventitious carbon peak as a reference. The low-resolution imaging of catalyst morphology was obtained with a transmission electron microscope (TEM) JEOL equipped with a LaB_6 emission gun and operating at 160 kV. High-resolution micrographs and STEM elemental mapping were acquired using a FEI Titan HRTEM microscope equipped with X-FEG electron gun operating at 80 kV. Absorbance spectra were measured using a UV−Vis spectrophotometer SPECORDS 600 (Analytik Jena). Absorption and extinction spectra were evaluated from transmittance and scattering measurements using a UV−vis−NIR spectrometer (Analytik Jena Specord 250 Plus) equipped with an integrating sphere (see Section S2). Electron energy loss imaging of free plasmons in TiN−Pt nanohybrids was recorded on a FEI-Titan (S)TEM operated at 300 kV, operating in the monochromated mode (with energy resolution 0.2 eV) and focusing on the low energy-loss regime to map the plasmonic modes of the nanohybrids.

Opto-Electronic and Photothermal Simulations. The simulations were carried out using classical thermo-electrodynamics with COMSOL Multiphysics, with the objective to study the opto-electronic and photothermal properties of our plasmonic materials. Our model consisted of a 40 nm TiN nanocube with a corner radius of 8 nm in water. Additionally, sixteen Pt semispheres, with a diameter equal to 3.3 nm, were evenly distributed on each nanocube face. These parameters were chosen to best replicate the nanoparticles utilized in the experiment. The thermal coefficients corresponding to each material are included in Table S7.

The calculations assumed an average of incident wave planes over all orientations and a large interparticle distance to avoid coupling. The system was set up to be at an ambient temperature (T_{amb}) of 293.15 K before calculating its temperature increment. Using these conditions, the calculations included the absorption, scattering, and extinction cross-sections, the field enhancement factor, and the temperature increment of the TiN−Pt nanohybrids. Finally, a plain TiN nanocube was modeled to make a comparison and to observe the contribution of the Pt nanocrystals.

To produce photothermal calculations, the model relied on the heat transfer equation expressed as

$$\rho(\vec{r})c(\vec{r})\frac{\partial T(\vec{r},t)}{\partial t} = \vec{\nabla}\cdot(k(\vec{r})\vec{\nabla}T(\vec{r},t)) + q(\vec{r},t)$$

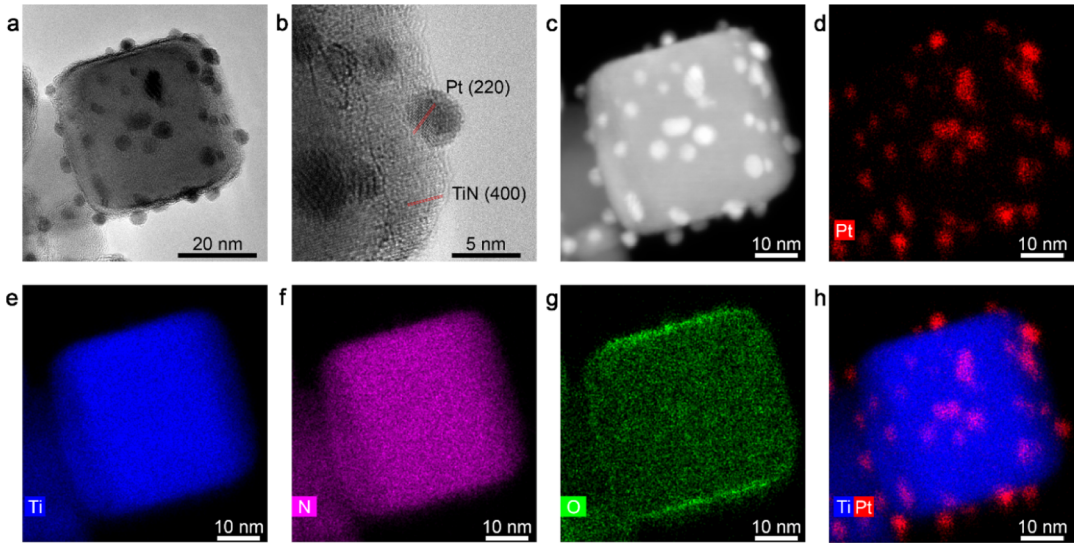

Figure 1. (a) Representative TEM image of a single TiN−Pt system where Pt nanocrystals are uniformly distributed over a TiN nanocube. (b) Magnified high-resolution TEM image showing lattice fringes of TiN and Pt. (c−h) Dark-field STEM image of a representative TiN−Pt nanohybrid and EDS elemental maps of Pt (d), Ti (e), N (f), O (g), and an overlay of Ti and Pt (h) showing the spatial distribution of Pt nanocrystals over TiN nanocubes.

where $T(\vec{r},t)$ is the temperature increase as a function of the coordinate $\vec{r}$ and time t. The coefficients $\rho(\vec{r})$, $c(\vec{r})$, $k(\vec{r})$ are the mass density, specific heat, and thermal conductivity, respectively. The function $q(\vec{r},t)$ is the local heat source generated by the light dissipation of the nanoparticle, and it is given by

$$q(\vec{r},\,t) = \langle \vec{j}\,(\vec{r},\,t)\cdot\vec{E}(\vec{r},\,t)\rangle_t = \mathrm{Im}(\varepsilon_{\mathrm{NP}})\frac{\omega\varepsilon_0}{2}\vec{E}_\omega\cdot\vec{E}_\omega^*$$

where ε_0 is the dielectric permittivity in vacuum, $\mathrm{Im}(\varepsilon_{\mathrm{NP}})$ is the imaginary part of the permittivity of the nanoparticle, and E_ω is the electric field inside the nanoparticle. We are then able to obtain a temperature difference defined as

$$\Delta T = T - T_{\mathrm{amb}}$$

where T_{amb} is the ambient temperature.

Hydrogen Evolution Experiments from Ammonia Borane. DI-H_2O (22 mL) was added to 2.4 mg of reduced TiN−Pt nanohybrids in a 25 mL round-bottom flask. The catalyst was dispersed by sonicating the solution for 5 min. The catalyst solution was then irradiated under solar-simulated light (Sciencetech Light Line A4-C250 equipped with an AM 1.5G filter, class CAA) with different intensities (from 1 to 10 suns, i.e., from 100 to 1000 mW cm^{-2}) for 5 min under stirring to homogenize the temperature in the solution. The different light intensities were calibrated with a thermopile detector (Standa 11UP19-H) before each experiment. The light beam area impinging on the photoreactor was 4 cm^2. The solution temperature was measured with a thermometer. Then, an aqueous ammonia borane (NH_3BH_3, Sigma-Aldrich) solution (0.28 mmol in 1 mL of water) was injected into the catalyst solution using a micropipette. The volume of evolved hydrogen gas was measured using an inverted water-filled burette connected to the reaction flask through inserting a rubber tube. The volume of the evolved hydrogen gas was monitored by recording the displacement of water in the gas burette. Completion of the reaction was confirmed when gas generation stopped. The wavelength-dependent H_2 evolution experiments were carried out by employing optical band-pass filters (Thorlabs, fwhm = 10 nm) and using a power density of 2 mW cm^{-2} at all selected wavelengths.

Catalytic Reduction of 4-Nitrophenol. First, 8.5 mg of NH_3BH_3 and 3.5 mL of 0.2 mM 4-nitrophenol (NPh) aqueous solution were mixed in a 4 mL quartz cell equipped with a small magnetic stirrer. Then, a 0.229 mL of aqueous dispersion of TiN−Pt nanohybrids was added to the solution under the stirring condition. The molar ratio of Pt/4-NPh/NH_3BH_3 was adjusted to 1/61/24553. After adding the catalyst, the cuvette was sealed with the lid. The conversion of 4-NPh to 4-aminophenol was monitored by recording the UV−vis spectra at different time intervals in the range 250−550 nm. Based on the change in the intensity at λ = 400 nm as a function of time, the rate constant of the catalytic hydrogenation of 4-NPh was determined. The reaction was carried out under dark conditions and 5 sun illumination. The amount of catalyst was adjusted in such a way that it did not influence the UV−vis spectrum of 4-nitrophenoxide anion during the time-dependent study.

RESULTS AND DISCUSSION

Synthesis and Characterization of TiN−Pt Nanohybrids. We prepared TiN−Pt nanohybrids by developing a synthetic strategy that allows us to decorate each TiN nanocube (average size 41 ± 10 nm) with a multitude of Pt nanocrystals. In order to enhance the binding of Pt nanocrystals onto the surface of the plasmonic core, commercial TiN nanocubes were initially treated with concentrated HCl. Reacting potassium tetrachloroplatinate in the presence of a mild reducing agent (formaldehyde) and NaOH enabled the decoration of TiN nanocubes with well-separated Pt nanocrystals. The use of NaOH, which neutralizes the HCl evolved during the reduction of the Pt precursor, produced a higher number of Pt nucleation centers on the surface of TiN nanocubes, which eventually led to the uniform growth of small Pt nanocrystals. A final reduction step under H_2 flow at 200 °C for 2 h was applied to clean the Pt surface and boost the catalytic activity of plasmonic nanohybrids before running photocatalytic experiments (see the Exper-

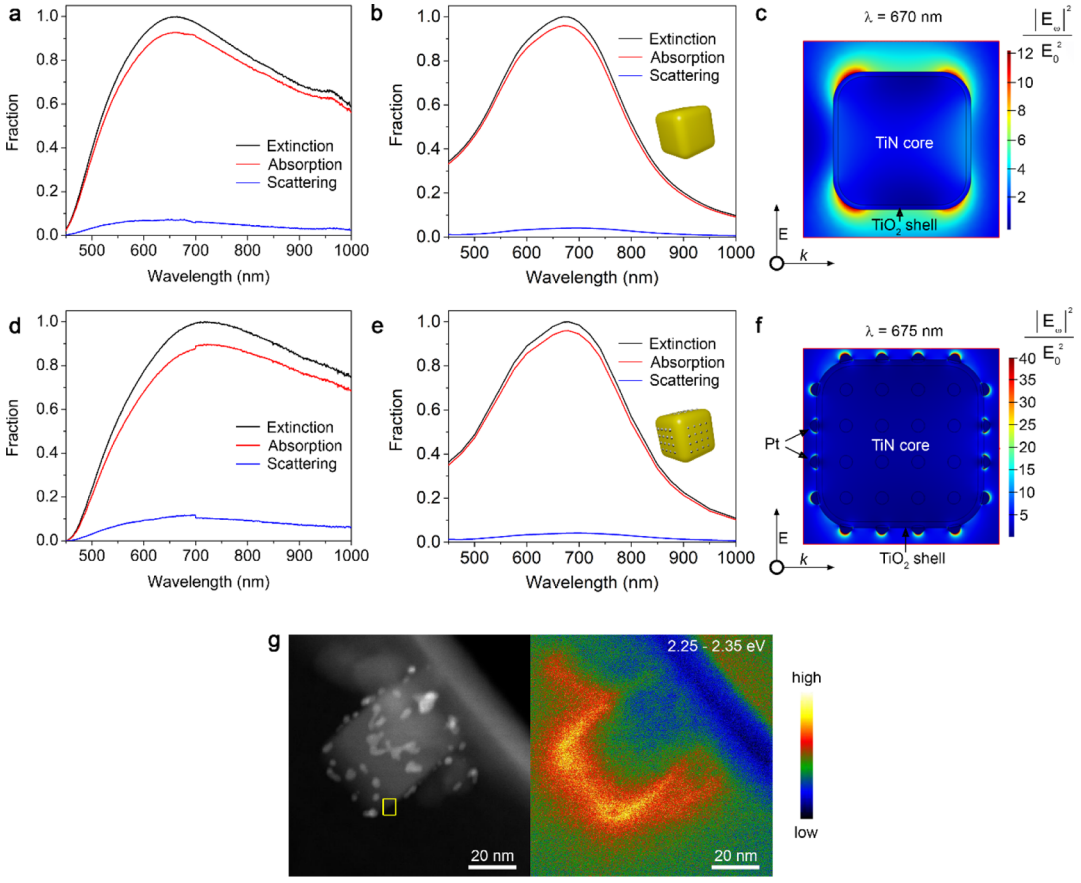

Figure 2. (a) Experimental extinction, absorption, and scattering of TiN nanocubes. (b) Calculated extinction, absorption, and scattering of TiN nanocubes including a 1.5 nm thick TiO_2 surface layer. (c) Electric field enhancement ($|E_\omega^2|/E_0^2$) distribution at 670 nm in a TiN nanocube. (d) Experimental extinction, absorption, and scattering of TiN−Pt nanohybrids including a 1.5 nm thick TiO_2 surface layer. (e) Calculated extinction, absorption, and scattering of TiN−Pt nanohybrids. (f) Electric field enhancement distributions at 675 nm in a TiN−Pt nanohybrid. (g) Dark-field STEM image of TiN−Pt nanohybrids on the Si_3N_4 membrane (left) and corresponding electron energy loss image (right) relative to the excitation of the dipolar plasmonic mode. The yellow square on the dark-field micrograph shows the focus of the electron beam.

imental Section and Section S1 in the Supporting Information for in-depth nanohybrids characterization).

Figure 1 shows the morphology of a representative reduced TiN−Pt nanohybrid. The high-resolution transmission electron micrographs (HRTEM, Figure 1a,b) evidence that Pt nanocrystals have an average size of 3.3 ± 0.3 nm and form a sharp interface with the external surface of the TiN nanocube.

The corresponding dark-field scanning TEM image and energy-dispersive X-ray spectroscopy (EDS) elemental mapping (Figure 1c−h) highlight that Pt nanocrystals grew homogenously around the TiN core, which retained a stoichiometric atomic distribution of Ti and N even after the Pt decoration and reduction treatment. Notably, oxygen elemental mapping (Figure 1g) clearly shows the presence of a 1.5 nm thick layer rich in oxygen, including a TiON/TiO_2 mixture as evidenced by X-ray photoemission spectroscopy analysis (Section S1 of the Supporting Information). This passivation layer is commonly formed in TiN nanostructures upon exposure to air and/or chemicals during the Pt nanocrystals deposition, which may act as a protective shell toward further oxidation.

Optical Properties of TiN−Pt Nanohybrids. The optical properties of pristine TiN and TiN−Pt nanohybrids were studied by measuring extinction, absorption, and scattering spectra in an aqueous solution (see details in Section S2). Figure 2a,d show that the decoration of TiN nanocubes with Pt nanocrystals induced a significant shift of the extinction peak from 664 to 720 nm as the result of the dielectric environment change at the surface of TiN because of the Pt deposition. Notably, TiN−Pt nanohybrids present a remarkable absorption fraction of about 0.9, while the scattering contribution is minimal, and it is similar for both pure TiN (0.07) and for TiN−Pt (0.10).

To gain further insights into the optical properties of TiN−Pt nanohybrids, we performed finite element method (COMSOL) simulations (see the Experimental Section). The calculated extinction, absorption, and scattering for a pure TiN nanocube (40 nm) and TiN nanocube decorated with sixteen Pt nanocrystals per facet are shown in Figure 2b,e. Both models include a 1.5 nm thick TiO_2 surface layer on top of TiN. The simulated optical properties agree well with the experimental measurements, confirming the large absorption fraction and low scattering. The electromagnetic simulations match very well the LSPR peak of TiN nanocubes, with the simulated value (670 nm) being almost identical to the experimental one (664 nm). For the case of TiN−Pt nanohybrids, the simulated LSPR peak is instead at ∼675 nm and differs from the experimental value by only 45 nm. For the latter, the small difference between simulated and experimental spectra could be due to the partial aggregation of TiN−Pt in solution, with Pt NPs deposition that might favor this process if compared to the case without Pt.

Figure 2c,f compare the E-field enhancement at the surface of a TiN nanocube and a TiN−Pt nanohybrid induced by the resonant excitation of the dipolar LSPR. As expected, the electric fields in the TiN nanocube localize around the corners, while for the TiN−Pt nanohybrid, the optical energy is concentrated at the catalytic Pt surface. Interestingly, $|E_\omega^2|/E_0^2$ at the Pt/water interface is three times higher (~40) than that generated at the corners of the TiN nanocubes (~12).

To map the E-field distribution, we excite the free plasmon resonances in TiN−Pt nanohybrids deposited on a Si_3N_4-coated TEM grid and use dark-field scanning TEM (STEM) and electron energy loss spectroscopy (EELS). The EELS spectrum revealed the only presence of the dipolar plasmon resonance peaking at 2.25−2.35 eV (Section S2).

The difference in the energy position between the LSPR observed in optical measurement (1.72 eV) and the free plasmons excited with fast electrons might be due to the increased radiation damping of polaritons (LSPR) compared to the free plasmon, which lowers the resonance energy of the former (i.e., by almost 1 eV for 100 nm Ag nanoparticles).[43] Figure 2g shows the dark-field STEM micrograph and corresponding EELS mapping at an energy of 2.25−2.35 eV, showing that plasmonic electric fields propagate all over the Pt nanocrystals surface.

An ideal plasmonic antenna (optically active unit)−reactor (catalytically active unit) nanohybrid should maximize light absorption (e.g., generation of charge carriers) while suppressing the radiative decay channel (scattering) of LSPR.[44,45] For this reason, we selected a TiN nanocube size of ~40 nm, which showed absorption as the dominant mechanism of the light−matter interaction. However, in order to assess the location of hot electron generation and the reaction mechanism, it is also crucial to determine whether absorption is spatially localized in the plasmonic core (TiN) or in the catalytic material (Pt). In the first case, hot electrons may be generated in the plasmonic material and then transferred to the catalytic metal for participating in the chemical reaction. In another case, instead, hot carriers may be directly generated onto the catalytic metal surface being readily available for catalysis.

Chavez et al. showed that core−shell nanoparticles including a core made using a Ag nanocube and a shell composed of a catalytic metal (i.e., Pt) present peculiar optical properties where the plasmonic near field assists and promotes the optical transitions from the plasmonic material to the catalytic one.[46] This is possible in light of the high ratio (i.e., max. 15−20 at $\lambda \approx 700$ nm) between the imaginary parts of the dielectric permittivity of catalytic and traditional plasmonic materials (Au, Ag).[45,46]

In order to determine the spatial location of light absorption inside our TiN−(TiO_2)−Pt nanohybrids, we retrieved the simulated optical absorption cross-section in each constituent component (Figure 3). The theoretical curves show that TiN accounts for 96.51%, Pt nanoparticles for 3.26%, and TiO_2 for 0.03% of the total absorption (Figure 3a). The lower fraction of the total absorption related to the catalytic metal (Pt) in our nanohybrids is expected because the total volume of the Pt nanoparticles is small as compared to the TiN volume and, in addition, Pt possesses relatively small values for the imaginary part of the dielectric permittivity at visible wavelengths.

More information about light absorption inside the Pt nanoparticles can be obtained by computing the absorption for one single Pt nanoparticle inside the TiN−Pt nanohybrid ($\sigma_{abs,Pt,TiN-Pt,per\ one\ particle}$) and for an isolated Pt nanoparticle ($\sigma_{abs,Pt,isolated\ Pt}$) (Figure 3b). Then, we define the ratio of the absorption cross-sections:

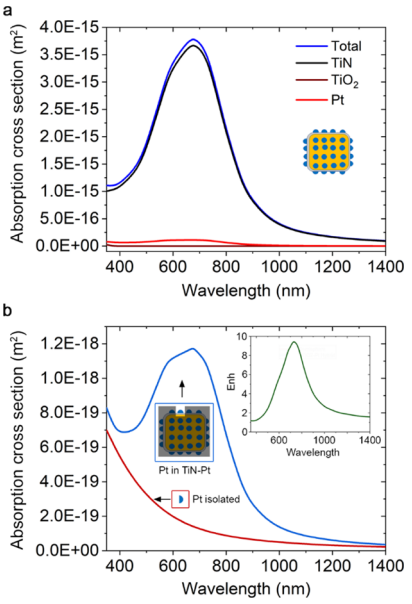

Figure 3. (a) Simulated absorption cross-sections for the complete TiN−Pt nanohybrid (blue line), and for each single component: TiN (black line), TiO_2 (brown line), and Pt (red line). (b) Simulated absorption cross-section for a single, isolated Pt nanoparticle (red line), and for a single Pt nanoparticle inside the TiN−Pt nanohybrid (blue line). The model for the Pt nanoparticle is a semi-sphere. Inset: absorption cross-section enhancement for a Pt nanoparticle inside the TiN−Pt nanohybrid.

$$\mathrm{Enh}(\lambda) = \frac{\sigma_{abs,Pt,TiN-Pt,per\ one\ particle}(\lambda)}{\sigma_{abs,Pt,isolated\ Pt}(\lambda)} \quad (2)$$

where the absorption per one Pt particle inside the TiN−Pt hybrid is given by

$$\sigma_{abs,Pt,TiN-Pt,per\ one\ particle}(\lambda) = \frac{\sigma_{abs,Pt,TiN-Pt}(\lambda)}{96} \quad (3)$$

In our model, we assume that one nanohybrid contains 96 Pt semi-spheres. The ratio (2) is, in fact, a plasmonic enhancement factor for our hybrid nanomaterial. Figure 3b shows that $\sigma_{abs,Pt,TiN-Pt,per\ one\ particle}$ for one single Pt nanoparticle inside the TiN−Pt nanohybrid is strongly enhanced when compared to $\sigma_{abs,Pt,isolated\ Pt}(\lambda)$ of an isolated Pt nanoparticle, with a maximum Enh ≈ 10 at 730 nm. However, the photocatalytic experiments are done with the solar-like spectrum, and the enhancement coefficient for the absorptions should be computed considering the extended spectrum of excitation (see the Supporting Information). For solar light, we obtain $\mathrm{Enh}_{solar} \approx 3.3$.

Hydrogen Evolution from NH_3BH_3 Dehydrogenation. We describe the photocatalytic performance of TiN−Pt nanohybrids for plasmon-enhanced H_2 evolution using conventional figures of merit utilized in heterogeneous catalysis and photocatalysis such as the turnover frequency (TOF in $mol_{H_2}\ mol_{Pt}^{-1}\ min^{-1}$) and apparent quantum yield (AQY % in molecules/photons). Photocatalytic performance is always expressed as a difference between photothermal (light) and thermal (dark) reaction rates. An exhaustive description about

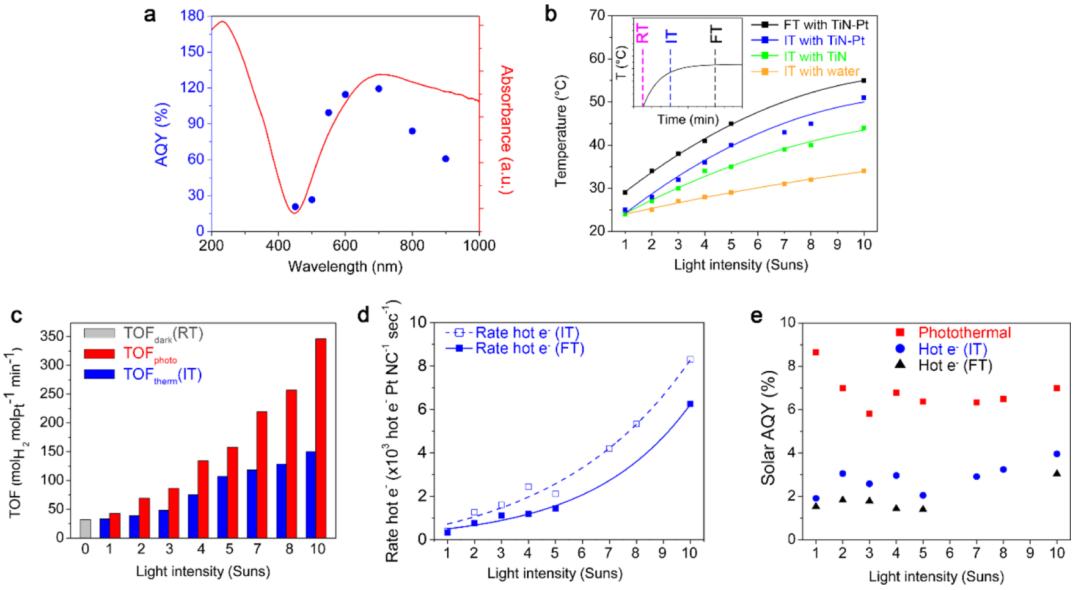

Figure 4. (a) AQYs for H_2 evolution from NH_3BH_3 dehydrogenation over TiN−Pt under monochromatic light (blue dots) and TiN−Pt absorption spectrum (red line). (b) Experimental temperatures generated in the photocatalytic reactor under different solar intensities: FT with TiN−Pt nanohybrids and ITs with TiN−Pt, TiN, and water. The inset defines IT as the temperature generated after 5 min of irradiation, whereas FT as the temperature registered at the end of the reaction. (c) TOF of H_2 evolution from NH_3BH_3 dehydrogenation over TiN−Pt nanohybrids in dark at RT, in dark at intermediate temperature (IT) TOF_{therm}, and under AM 1.5G solar irradiation (photothermal, TOF_{photo}) at different light intensities (1 sun = 100 mW cm^{-2}). (d) Hot electron generation rate at both IT and FT under solar irradiation. (e) AQYs for H_2 evolution from NH_3BH_3 dehydrogenation over TiN−Pt under solar irradiation.

the calculation of catalytic figures of merit is reported in the Supporting Information Section S3.

When we tested our nanohybrids in the plasmon-enhanced H_2 evolution from NH_3BH_3 dehydrogenation, we did not observe any considerable H_2 generation rate in the absence of the catalyst nor by the addition of TiN nanocrystals into the aqueous NH_3BH_3 solution and under light irradiation. In contrast, we detected H_2 evolution only when using TiN−Pt nanohybrids (both in dark and light), suggesting that the presence of Pt is mandatory to activate NH_3BH_3 dehydrogenation.

Furthermore, to evaluate the photocatalytic properties of Pt nanocrystals, we synthesized 1.8 nm Pt nanocrystals supported on optically inactive Al_2O_3 (see Figure S14) and tested them in the photocatalytic hydrogen evolution from ammonia borane dehydrogenation under 5 suns illumination and in the dark at photothermal conditions [at final temperature (FT) generated under 5 suns]. The reaction kinetics obtained under light and dark conditions (Figure S14d) showed an identical reaction time for producing 3 mol equivalent of H_2. This finding confirmed that Pt nanocrystals had no significant contribution as a photocatalyst during the light-assisted ammonia borane dehydrogenation, as instead previously observed during CO photothermal oxidation over Pt/Al_2O_3.[47]

To demonstrate that plasmonic hot electrons enhance H_2 evolution from NH_3BH_3 dehydrogenation, we performed wavelength-dependent catalytic runs. We selected light with a power density of 2 mW cm^{-2} at all wavelengths, such that the solution temperature did not deviate from RT along the course of the reaction, that is, no effect of photothermal heating.

TiN−Pt nanohybrids show a TOF value of 32.1 mol_{H_2} mol_{Pt}^{-1} min^{-1} in dark at RT (in line with the best monometallic Pt catalysts reported in the literature, see Table S6), while in light conditions, we observed increased H_2 production rates at all investigated wavelengths (450−900 nm). We calculated AQYs under monochromatic light by using the reaction rate difference between light and dark conditions. Figure 4a shows the photocatalytic AQY at different wavelengths along with the absorption spectrum of TiN−Pt nanohybrids. The photocatalytic AQY action spectrum closely followed the absorption of TiN−Pt, thus confirming that AQY is related to light absorption in the reaction mixture, which can induce both hot electron and photothermal plasmonic catalysis.[24,48,49] In this case, however, we avoid photothermal heating using low light intensity, and therefore, the reported AQYs are due to the action of plasmonic hot electrons. Notably, we obtained very high AQYs in all range of investigated wavelengths, with AQYs exceeding 100% for experiments carried out at wavelengths (550, 600, 700 nm) around the LSPR of TiN−Pt nanohybrids.

The highest AQY (120%) was observed when light exactly matched the LSPR maximum at 700 nm. Our values are among the highest AQYs ever reported for plasmonic photocatalysis in liquid media. For instance, plasmonic systems for liquid-phase reactions have shown modest AQYs reaching 20% for H_2 evolution from methylene blue and trifluoroacetic acid with $Au/TiO_2/Ru$,[50] and 18% for the aerobic oxidation of 2-propanol to acetone with $AuCu/TiO_2$.[51] In contrast, for gas-phase reactions, AQYs have reached values as high as 800% (using monochromatic light at 400 mW cm^{-2}, i.e., 200 times more intense than our light source),[36] 60% for the partial oxidation of ethylene with Ag/Al_2O_3,[24] 33.5% for ammonia decomposition to H_2 with $Cu−Ru/MgO$,[35] and 10% for the photocatalytic oxidation of CO with $Ag@SiO_2/Pt$.[44]

The observed high AQYs may be due to the high absorption of TiN−Pt nanohybrids and the modest energy barrier of the targeted chemical reaction. This allows us to make use not only of highly energetic hot electrons but eventually also of those electrons with lower energy,[17] that is, hot electrons that already

underwent inelastic scattering before reacting with the NH_3BH_3 molecules.

In order to further investigate the efficiency of TiN−Pt nanohybrids in plasmon-enhanced H_2 evolution, we performed NH_3BH_3 dehydrogenation under AM 1.5G solar illumination using different light intensities. In contrast to experiments carried out with monochromatic light, solar illumination always produced an increase in temperature because of photothermal heating (Figure 4b). To distinguish how the increase in temperature and how hot electrons affect H_2 evolution kinetics, we first measured the temperature increase due to light irradiation in the reacting solution, performed catalytic experiments in dark conditions at each specific "photothermal" temperature, and then subtracted this contribution to the H_2 evolution rates observed under light irradiation (see detailed explanation in the Supporting Information, Section S3).

The correct measurement of photothermal temperature generated on the surface of plasmonic catalysts can be challenging, especially in case of gas-phase chemical reactions driven using solid bed catalysts.[48,49] Otherwise, in colloidal photocatalysis (as in our case), contact between individual nanoparticles and the liquid medium ensures effective heat removal by conduction/convection. In such a system, the difference between the nanoparticle surface temperature and the bulk temperature can be reduced to an insubstantial magnitude.[48] This validates that our methodology to measure photothermal heating in the reacting solution by the use of a thermocouple well approximate the measurements of the real temperature generated at TiN−Pt nanohybrids' surface.

In the presence of TiN−Pt, solar irradiation produced substantial heating in the reaction solution, reaching temperatures of ∼50 °C under 10 suns. To avoid excess of heating, which may over accelerate NH_3BH_3 dehydrogenation, we defined a plasmonic IT and a FT as the collective temperatures (because of all the nanohybrids used for catalysis) generated after 5 min of light irradiation and at the end of reaction, respectively (Figure 4b). Figure 4b shows the evolution of temperature under increasing light intensity for different experimental conditions and highlights that IT accounted generally for 80−85% of FT.

To analyze the photocatalytic performance of our nanohybrids, we divide the TOF into two parts

$$\mathrm{TOF}_{\mathrm{photo}}(H) = \mathrm{TOF}_{\mathrm{therm}}(H) + \mathrm{TOF}_{\mathrm{hot\text{-}e}}(H) \quad (4)$$

where $\mathrm{TOF}_{\mathrm{photo}}$ is the overall photothermal H_2 evolution rate, $\mathrm{TOF}_{\mathrm{therm}}$ is the thermal contribution, and $\mathrm{TOF}_{\mathrm{hot\text{-}e}}$ is the contribution coming from nonthermalized energetic electrons (hot electrons) at a given light intensity (H). Because we can measure $\mathrm{TOF}_{\mathrm{photo}}$ and $\mathrm{TOF}_{\mathrm{therm}}$, we can retrieve their difference that represents the contribution of hot electrons, $\mathrm{TOF}_{\mathrm{hot\text{-}e}}$.

Figure 4c shows the $\mathrm{TOF}_{\mathrm{therm}}$ (at IT) values under dark and $\mathrm{TOF}_{\mathrm{photo}}$ obtained under solar irradiation at different light intensity. In-depth kinetic study was carried out for H_2 generation during NH_3BH_3 dehydrogenation reaction catalyzed by our reduced TiN−Pt nanohybrids under different light intensities and different ITs and FTs in the dark, as shown in Figure S16. Notably, when we introduced solar irradiation, we observed a nonlinear increase of $\mathrm{TOF}_{\mathrm{photo}}$ with light intensity. At 10 suns illumination, $\mathrm{TOF}_{\mathrm{photo}}$ reached 346.1 $\mathrm{mol}_{H_2}\ \mathrm{mol}_{Pt}^{-1}\ \mathrm{min}^{-1}$, with TiN−Pt showing, therefore, a ∼11-fold enhancement in catalytic activity with respect to dark conditions because of the combined effect of photothermal heating and hot electrons. Interestingly, the heating contribution considering IT ($\mathrm{TOF}_{\mathrm{therm}}$, Figure 4c, blue bars) is prominent at low light irradiation, while it becomes less than 50% the $\mathrm{TOF}_{\mathrm{photo}}$ value at 10 suns. In other words, the hot electron effect is more prominent at increasing light intensity.[24,35,44,52] The same trend is also observed when considering FT, as shown in Figure S16.

To further elucidate the role of local heating and hot electrons, we calculated $\mathrm{TOF}_{\mathrm{hot\text{-}e}}$ at both ITs and FTs[44] (see the Supporting Information, Section S3) and then the hot electron generation rate per Pt nanocrystal at different light intensities (Figure 4d). Notably, the temperature increase in the reacting solution is dynamic during the course of reaction; therefore, $\mathrm{TOF}_{\mathrm{hot\text{-}e}}$ values obtained using $\mathrm{TOF}_{\mathrm{therm}}$ at ITs (minimum photothermal heating) and FTs (maximum photothermal heating) represent the maximum and the minimum number of useable hot electrons participating to H_2 evolution, respectively.

Figure 4d shows that the hot electron generation rate during plasmon-enhanced H_2 evolution from NH_3BH_3 dehydrogenation exhibits a superlinear, power-law dependence from light intensity, a characteristic feature observed in electron-driven chemical reactions on metals.[20,52]

Figure 4e shows the solar AQYs for photothermal and hot electron-driven rates for plasmon-enhanced H_2 production. The photothermal solar AQY is ∼9% at 1 sun and decreases to stable values comprised between 6 and 7% at higher light intensities. In contrast, the hot electron (either considering IT or FT) solar AQY trend shows similar values around 2−3% up to 5 suns illumination, while for higher light intensity, it increases to ∼4% at 10 suns illumination. Plots of AQYs highlight that at low light intensity (1−5 suns), photothermal effects play a major role in boosting the activity of TiN−Pt nanohybrids, while at higher intensity (5−10 suns), the contribution from hot electrons prevails over heating.[35]

We also evaluated the recyclability and stability of the reduced TiN−Pt nanohybrids in the NH_3BH_3 dehydrogenation reaction. The catalytic performance of the nanohybrids was comparable after three consecutive catalytic cycles (Figure S18). The TEM image and photograph of reused nanohybrids show that the size, morphology, and their colloidal stability remain unaltered after catalytic reactions, confirming their high stability and recyclability (Figure S19).

Theoretical COMSOL Simulations. To further demonstrate that the reaction rates are influenced by collective photothermal heating[53,54] rather than by thermal gradients generated nearby a single nanostructure, we performed COMSOL simulations and calculated the increase in temperature caused by a single TiN−Pt nanohybrid, always considering a 1.5 nm surface layer of TiO_2. We started from the case of a single nanohybrid under monochromatic excitation with a relatively high intensity (Figure 5) and observed relatively small values for the local photo-induced temperature even for such high intensity.

Regarding our experiments with solar-like radiation, the total temperature increase near a single nanohybrid (NH) can be divided in two parts as follows:

$$\Delta T_{\mathrm{photo}}(r) = \Delta T_{\mathrm{collective}} + \Delta T_{\mathrm{local}}(r) \quad (5)$$

where $\Delta T_{\mathrm{collective}}$ and $\Delta T_{\mathrm{local}}$ are the collective and local temperatures, respectively. The contribution $\Delta T_{\mathrm{collective}}$ comes

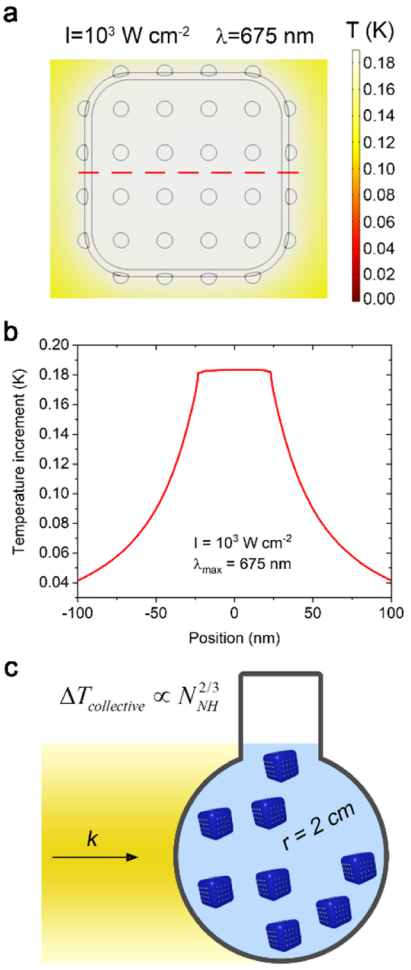

Figure 5. (a) Temperature map of a single TiN−Pt nanohybrid with a 1.5 nm surface layer of TiO_2 and (b) corresponding distance-dependent temperature profile. In (a,b), the optical excitation is monochromatic, at the wavelength at the plasmon peak. (c) Schematic representation of the photocatalytic reactor showing the dependence of collective heating from the number of nanoparticles.

from all neighboring nanohybrids and does not significantly change in space in the vicinity of the considered nanohybrid. As expected, the COMSOL-calculated local temperature increase nearby a single TiN−Pt nanohybrid, ΔT_{local}, is very small and it is estimated to be 8.1×10^{-6} °C under 1 sun illumination. Overall, the calculated local temperature increase in our system scales linearly with the light intensity

$$\Delta T_{local} = T_1 \cdot I_{sun}$$

where I_{sun} is the light intensity in suns. Details of our numerical estimation for the solar local temperature increase can be found in the Supporting Information. Notably, even under resonant illumination (λ = 675 nm) at $I = 10^3$ W cm^{-2}, that is, much higher than the experimental light intensity, the temperature increase on the surface of TiN−Pt is only ~0.2 K and decreases rapidly with the distance from the nanohybrid surface (Figure 5a,b).

The photo-induced temperature is proportional to the energy dissipation inside one nanohybrid and can be estimated analytically as

$$\Delta T_{local} \approx \frac{q_{NH,solar}}{4\pi k_{t,w}} \frac{1}{L_{NH}/2} \quad (6)$$

where $q_{NH,solar}$ is the total heat power dissipated in the nanohybrid under solar irradiation, and $k_{t,w}$ and L_{NH} are the thermal conductivity of water and the nanohybrid size, respectively. Section S4 contains more details on these photothermal calculations. In a large three-dimensional system, the collective temperature increases with the number of illuminated nanohybrids as[53] (Figure 5c)

$$\Delta T_{collective} = \text{Coeff} \cdot \Delta T_{local} N_{NH}^{2/3} \quad (7)$$

where N_{NH} is the total number of nanohybrids and Coeff is a coefficient dependent on the size and concentration of the nanocrystals. In our system, the number of nanohybrids is, of course, very large, and therefore, we have $\Delta T_{collective} \gg \Delta T_{local}$. Indeed, the measured temperature (i.e., collective temperature) is much higher than the calculated local one. However, a theoretical calculation of the collective temperature is beyond the scope of this study because it involves complex processes of heat transfer from the outside surface of the spherical glass reactor to air, including convection and heat diffusion.

As expected, the enhancement coefficient owing to the collective heating is a large number

$$\text{Enh}_T = \frac{\Delta T_{collective}}{\Delta T_{local}} = 0.6 \times 10^6 \quad (8)$$

where we used 1 sun illumination and $\Delta T_{collective}$ = 5 °C that is the temperature increase due to the TiN−Pt nanohybrid, as determined from the experiment in Figure 4b. This is an important property of solution ensembles of nanohybrids. Whereas the local temperature increase is small, the resulting collective temperature can be significant as experimentally measured (55 °C under 10 suns illumination). In our case, this collective photo-induced temperature leads to a significant activity enhancement of the thermal origin.

Hot Electron-Driven Reaction Mechanism. For the dehydrogenation of NH_3BH_3 over metallic catalysts, it has been reported that the rate-determining step (RDS) is the cleavage of O−H bond in water molecules.[9,10] In order to verify this hypothesis, we first experimentally confirmed that NH_3BH_3 is not involved in the RDS of H_2 evolution by observing that the reaction kinetics shows a zero-order dependence with NH_3BH_3 concentration (Supporting Information, Section S5).

Afterward, we demonstrated the direct involvement of water in the RDS by performing the kinetic isotope effect (KIE) experiments with deuterated water (D_2O). Figure 6a shows the H_2 evolution kinetics for TiN−Pt nanohybrids in dark conditions using H_2O or D_2O. The KIE (H_2O rate/D_2O rate) was 5.1 and confirmed that H_2O cleavage limits the reaction rate in NH_3BH_3 dehydrogenation. When we run KIE experiments under 8 suns illumination (Figure S24), we found a higher KIE value (5.57) as compared to dark conditions (5.10), a characteristic feature of hot electron-driven processes,[20] thus confirming that plasmonic hot electron play a role in accelerating the breaking of O−H bonds in water molecules during ammonia borane dehydrogenation.

To quantify the effect of illumination on the activation energy (E_a), we used the Arrhenius equation and plotted H_2 evolution thermal rates in dark conditions at varying plasmonic temperature, as well as photocatalytic rates expressed as difference between the photothermal and the thermal rates (Figure 6b and Supporting Information, Section S5).[35] Without light, E_a was 48.7 kJ mol^{-1} (0.5 eV), while it

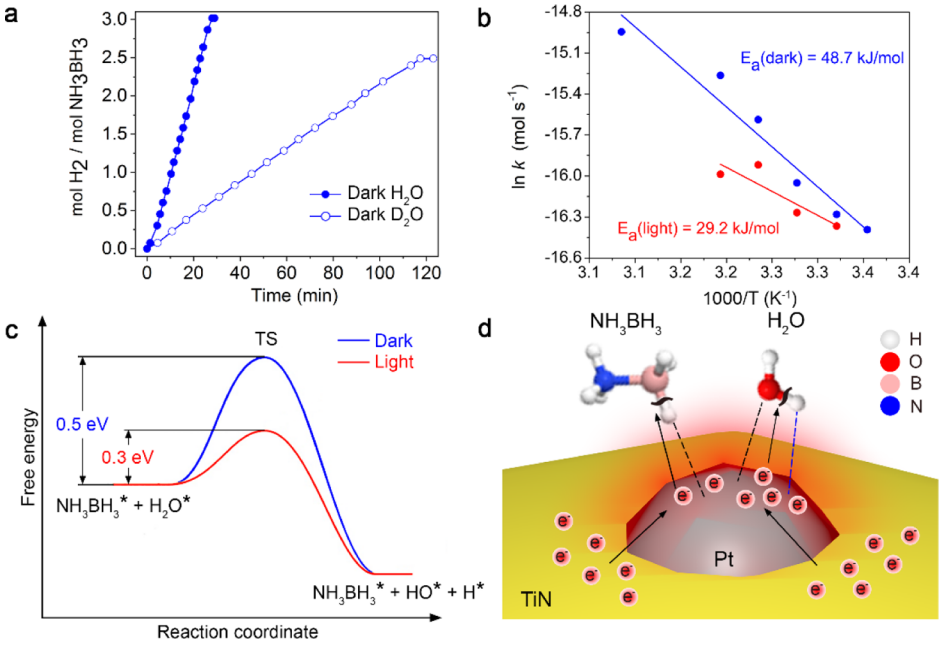

Figure 6. (a) Kinetics of H_2 evolution from ammonia borane (NH_3BH_3) dehydrogenation reaction with TiN−Pt nanohybrids in H_2O and D_2O in dark conditions. (b) Arrhenius plots of apparent activation energies under light and dark conditions at plasmonic temperature. k is the rate of H_2 evolution. (c) Schematic representation of the free energy plots showing the energy barriers associated with the formation of the reaction TS of the RDS during NH_3BH_3 dehydrogenation reaction under light and dark conditions. Asterisks denote species adsorbed on the catalyst surface. (d) Cartoon showing the facilitated rupture of O−H bond of the water molecule induced by plasmonic hot electrons generated on the surface of a TiN−Pt nanohybrids.

decreased to 29.2 kJ mol^{-1} (0.3 eV) under solar light irradiation. This suggests that hot electrons, produced upon TiN−Pt excitation, directly participate to the RDS of H_2 evolution (O−H bond cleavage) reaction by stabilizing the TS by 0.2 eV (Figure 6c,d). Hot electrons eventually accelerate the rupture of the B−H bond, thus finally enhancing the overall H_2 evolution rate (Figure S25, Section S5).

Plasmonic Tandem Hydrogenation of 4-Nitrophenol. We finally demonstrate the possibility of tandem hydrogenation of 4-nitrophenol using in situ-generated H_2 gas, evolved from plasmon-enhanced NH_3BH_3 dehydrogenation using TiN−Pt nanohybrids (Figure S26). Under dark conditions, the complete hydrogenation of 4-nitrophenoxide to 4-aminophenoxide anion takes 20 min in the presence of reduced TiN−Pt nanohybrids, whereas under 5 suns illumination, the reaction is completed in 6 min. The hydrogenation rate constants in the dark and under illumination is 0.17 and 0.42 min^{-1}, respectively, showing that plasmonic effects can produce a 2.5-fold rate enhancement during tandem hydrogenations reactions.

CONCLUSIONS

We reported the preparation of a plasmonic photocatalyst showing minimized scattering (0.1) and high absorption (0.9) including an acid-resistant plasmonic nanocubes core (TiN) and Pt nanocrystals. The generation of hot electrons is spatially localized mainly on the TiN core, while a smaller fraction of hot carriers is directly produced in the Pt catalytic centers. The plasmonic enhancement for the Pt-based photochemistry comes from three factors: very strong collective photo-heating created by the plasmonic TiN component, generation of hot electrons inside TiN (those electrons can propagate to the Pt component), and the threefold plasmonic enhancement of absorption inside the Pt nanoparticles (and in situ generation of hot electrons). We demonstrated that plasmonic nanohybrids can drive photocatalytic hydrogen evolution with 120% AQY under resonant optical excitation at 700 nm by harnessing hot electrons only. In contrast, when using solar simulated irradiation, TiN−Pt nanohybrids produced both efficient local heating and hot electron generation that boosted the TiN−Pt activity of more than one order of magnitude if compared to dark conditions, reaching a TOF of 346 mol_{H_2} mol_{Pt}^{-1} min^{-1} under 10 suns illumination. We further discerned the relative contributions of photothermal heating and hot electrons, showing that hot electrons play the role of decreasing the energy barrier to access the TS of the RDS by accelerating water splitting at the Pt surface. This work provides a general strategy to enhance the catalytic activity of transition metal catalysts for H_2 evolution from liquid feedstock through a combined action of heating and hot electrons, with important implications for H_2 storage technologies.

ASSOCIATED CONTENT

Supporting Information

The Supporting Information is available free of charge at https://pubs.acs.org/doi/10.1021/acscatal.0c00343.

Additional structural characterization, photocatalytic data, and theoretical plots (PDF)

AUTHOR INFORMATION

Corresponding Authors

Alexander O. Govorov − *Department of Physics and Astronomy, Nanoscale and Quantum Phenomena Institute, Ohio University, Athens, Ohio 45701, United States; Institute of Fundamental and Frontier Sciences, University of Electronic Science and Technology of China, Chengdu 610054, China;*

orcid.org/0000-0003-1316-6758; Email: govorov@ohio.edu

Alberto Naldoni − *Regional Centre of Advanced Technologies and Materials, Faculty of Science, Palacký University, Olomouc 78371, Czech Republic;* orcid.org/0000-0001-5932-2125; Email: alberto.naldoni@upol.cz

Authors

Sourav Rej − *Regional Centre of Advanced Technologies and Materials, Faculty of Science, Palacký University, Olomouc 78371, Czech Republic*

Luca Mascaretti − *Regional Centre of Advanced Technologies and Materials, Faculty of Science, Palacký University, Olomouc 78371, Czech Republic;* orcid.org/0000-0001-8997-7018

Eva Yazmin Santiago − *Department of Physics and Astronomy, Nanoscale and Quantum Phenomena Institute, Ohio University, Athens, Ohio 45701, United States*

Ondřej Tomanec − *Regional Centre of Advanced Technologies and Materials, Faculty of Science, Palacký University, Olomouc 78371, Czech Republic*

Štěpán Kment − *Regional Centre of Advanced Technologies and Materials, Faculty of Science, Palacký University, Olomouc 78371, Czech Republic*

Zhiming Wang − *Institute of Fundamental and Frontier Sciences, University of Electronic Science and Technology of China, Chengdu 610054, China*

Radek Zbořil − *Regional Centre of Advanced Technologies and Materials, Faculty of Science, Palacký University, Olomouc 78371, Czech Republic;* orcid.org/0000-0002-3147-2196

Paolo Fornasiero − *Department of Chemical and Pharmaceutical Sciences, INSTM and ICCOM-CNR, University of Trieste, Trieste 34127, Italy;* orcid.org/0000-0003-1082-9157

Complete contact information is available at: https://pubs.acs.org/10.1021/acscatal.0c00343

Author Contributions

S.R. synthesized nanohybrids, performed photocatalytic experiments, and wrote the draft of the manuscript. L.M. carried out optical measurements. E.Y.S. and A.O.G. designed and performed simulations, wrote the theoretical part of the manuscript. O.T. performed electron microscopy and EELS measurements. Š.K., Z.W., R.Z., and P.F. discussed results and revised the manuscript. A.N. conceived the concept, revised the manuscript, and supervised the project.

Notes

The authors declare no competing financial interest.

■ ACKNOWLEDGMENTS

The authors gratefully acknowledge the support from the Czech Science Foundation (GACR) through the project 20-17636S. Part of this work was carried out with the support of the CEITEC Nano Research Infrastructure (MEYS CR, 2016−2019).

■ REFERENCES

(1) Marder, T. B. Will We Soon be Fueling Our Automobiles with Ammonia−borane? *Angew. Chem., Int. Ed.* **2007**, *46*, 8116−8118.

(2) Rossin, A.; Peruzzini, M. Ammonia−borane and Amine−borane Dehydrogenation Mediated by Complex Metal Hydrides. *Chem. Rev.* **2016**, *116*, 8848−8872.

(3) Staubitz, A.; Robertson, A. P. M.; Manners, I. Ammonia−Borane and Related Compounds as Dihydrogen Sources. *Chem. Rev.* **2010**, *110*, 4079−4124.

(4) Sutton, A. D.; Burrell, A. K.; Dixon, D. A.; Garner, E. B., III; Gordon, J. C.; Nakagawa, T.; Ott, K. C.; Robinson, J. P.; Vasiliu, M. Regeneration of Ammonia−borane Spent Fuel by Direct Reaction with Hydrazine and Liquid Ammonia. *Science* **2011**, *331*, 1426−1429.

(5) Zhan, W.-W.; Zhu, Q.-L.; Xu, Q. Dehydrogenation of Ammonia−borane by Metal Nanoparticle Catalysts. *ACS Catal.* **2016**, *6*, 6892−6905.

(6) Chen, W.; Ji, J.; Duan, X.; Qian, G.; Li, P.; Zhou, X.; Chen, D.; Yuan, W. Unique Reactivity in Pt/CNT Catalyzed Hydrolytic Dehydrogenation of Ammonia−borane. *Chem. Commun.* **2014**, *50*, 2142−2144.

(7) Chandra, M.; Xu, Q. Room Temperature Hydrogen Generation from Aqueous Ammonia−borane Using Noble Metal Nano-Clusters as Highly Active Catalysts. *J. Power Sources* **2007**, *168*, 135−142.

(8) Aijaz, A.; Karkamkar, A.; Choi, Y. J.; Tsumori, N.; Rönnebro, E.; Autrey, T.; Shioyama, H.; Xu, Q. Immobilizing Highly Catalytically Active Pt Nanoparticles Inside the Pores of Metal−organic Framework: A Double Solvents Approach. *J. Am. Chem. Soc.* **2012**, *134*, 13926−13929.

(9) Li, Z.; He, T.; Matsumura, D.; Miao, S.; Wu, A.; Liu, L.; Wu, G.; Chen, P. Atomically Dispersed Pt on the Surface of Ni Particles: Synthesis and Catalytic Function in Hydrogen Generation from Aqueous Ammonia−borane. *ACS Catal.* **2017**, *7*, 6762−6769.

(10) Fu, F.; Wang, C.; Wang, Q.; Martinez-Villacorta, A. M.; Escobar, A.; Chong, H.; Wang, X.; Moya, S.; Salmon, L.; Fouquet, E.; Ruiz, J.; Astruc, D. Highly Selective and Sharp Volcano−type Synergistic Ni_2Pt@ZIF-8-Catalyzed Hydrogen Evolution from Ammonia−borane Hydrolysis. *J. Am. Chem. Soc.* **2018**, *140*, 10034−10042.

(11) Akbayrak, S.; Tonbul, Y.; Özkar, S. Ceria Supported Rhodium Nanoparticles: Superb Catalytic Activity in Hydrogen Generation from the Hydrolysis of Ammonia−borane. *Appl. Catal., B* **2016**, *198*, 162−170.

(12) Rej, S.; Hsia, C.-F.; Chen, T.-Y.; Lin, F.-C.; Huang, J.-S.; Huang, M. H. Facet-Dependent and Light-Assisted Efficient Hydrogen Evolution from Ammonia−borane Using Gold-Palladium Core-Shell Nanocatalysts. *Angew. Chem., Int. Ed.* **2016**, *55*, 7222−7226.

(13) Fuku, K.; Hayashi, R.; Takakura, S.; Kamegawa, T.; Mori, K.; Yamashita, H. The Synthesis of Size- and Color-Controlled Silver Nanoparticles by Using Microwave Heating and Their Enhanced Catalytic Activity by Localized Surface Plasmon Resonance. *Angew. Chem., Int. Ed.* **2013**, *52*, 7446−7450.

(14) Cheng, H.; Qian, X.; Kuwahara, Y.; Mori, K.; Yamashita, H. A Plasmonic Molybdenum Oxide Hybrid with Reversible Tunability for Visible-Light-Enhanced Catalytic Reactions. *Adv. Mater.* **2015**, *27*, 4616−4621.

(15) Verma, P.; Kuwahara, Y.; Mori, K.; Yamashita, H. Synthesis and Characterization of a Pd/Ag Bimetallic Nanocatalyst on SBA-15 Mesoporous Silica as a Plasmonic Catalyst. *J. Mater. Chem. A* **2015**, *3*, 18889−18897.

(16) Yin, H.; Kuwahara, Y.; Mori, K.; Yamashita, H. Plasmonic Metal/$Mo_xW_{1-x}O_{3-y}$ for Visible-Light-Enhanced H_2 Production from Ammonia−borane. *J. Mater. Chem. A* **2018**, *6*, 10932−10938.

(17) Govorov, A. O.; Zhang, H.; Gun'ko, Y. K. Theory of Photoinjection of Hot Plasmonic Carriers from Metal Nanostructures into Semiconductors and Surface Molecules. *J. Phys. Chem. C* **2013**, *117*, 16616−16631.

(18) Besteiro, L. V.; Kong, X.-T.; Wang, Z.; Hartland, G.; Govorov, A. O. Understanding Hot-Electron Generation and Plasmon Relaxation in Metal Nanocrystals: Quantum and Classical Mechanisms. *ACS Photonics* **2017**, *4*, 2759−2781.

(19) Manjavacas, A.; Liu, J. G.; Kulkarni, V.; Nordlander, P. Plasmon-Induced Hot Carriers in Metallic Nanoparticles. *ACS Nano* **2014**, *8*, 7630−7638.

(20) Christopher, P.; Xin, H.; Linic, S. Visible-Light-Enhanced Catalytic Oxidation Reactions on Plasmonic Silver Nanostructures. *Nat. Chem.* **2011**, *3*, 467−472.
(21) Wang, F.; Li, C.; Chen, H.; Jiang, R.; Sun, L.-D.; Li, Q.; Wang, J.; Yu, J. C.; Yan, C.-H. Plasmonic Harvesting of Light Energy for Suzuki Coupling Reactions. *J. Am. Chem. Soc.* **2013**, *135*, 5588−5601.
(22) Aslam, U.; Rao, V. G.; Chavez, S.; Linic, S. Catalytic Conversion of Solar to Chemical Energy on Plasmonic Metal Nanostructures. *Nat. Catal.* **2018**, *1*, 656−665.
(23) Naldoni, A.; Shalaev, V. M.; Brongersma, M. L. Applying Plasmonics to a Sustainable Future. *Science* **2017**, *356*, 908−909.
(24) Christopher, P.; Xin, H.; Marimuthu, A.; Linic, S. Singular Characteristics and Unique Chemical Bond Activation Mechanisms of Photocatalytic Reactions on Plasmonic Nanostructures. *Nat. Mater.* **2012**, *11*, 1044−1050.
(25) Marimuthu, A.; Zhang, J.; Linic, S. Tuning Selectivity in Propylene Epoxidation by Plasmon Mediated Photo-Switching of Cu Oxidation State. *Science* **2013**, *339*, 1590−1593.
(26) Swearer, D. F.; Zhao, H.; Zhou, L.; Zhang, C.; Robatjazi, H.; Martirez, J. M. P.; Krauter, C. M.; Yazdi, S.; McClain, M. J.; Ringe, E.; Carter, E. A.; Nordlander, P.; Halas, N. J. Heterometallic Antenna−Reactor Complexes for Photocatalysis. *Proc. Natl. Acad. Sci. U.S.A.* **2016**, *113*, 8916−8920.
(27) Kumari, G.; Zhang, X.; Devasia, D.; Heo, J.; Jain, P. K. Watching Visible Light-Driven CO_2 Reduction on a Plasmonic Nanoparticle Catalyst. *ACS Nano* **2018**, *12*, 8330−8340.
(28) Yu, S.; Jain, P. K. Plasmonic Photosynthesis of C_1−C_3 Hydrocarbons from Carbon Dioxide Assisted by an Ionic Liquid. *Nat. Commun.* **2019**, *10*, 2022.
(29) Yu, S.; Wilson, A. J.; Heo, J.; Jain, P. K. Plasmonic Control of Multi-Electron Transfer and C−C Coupling in Visible-Light-Driven CO_2 Reduction on Au Nanoparticles. *Nano Lett.* **2018**, *18*, 2189−2194.
(30) Robatjazi, H.; Zhao, H.; Swearer, D. F.; Hogan, N. J.; Zhou, L.; Alabastri, A.; McClain, M. J.; Nordlander, P.; Halas, N. J. Plasmon-Induced Selective Carbon Dioxide Conversion on Earth-Abundant Aluminum-Cuprous Oxide Antenna-Reactor Nanoparticles. *Nat. Commun.* **2017**, *8*, 27.
(31) DuChene, J. S.; Tagliabue, G.; Welch, A. J.; Cheng, W.-H.; Atwater, H. A. Hot Hole Collection and Photoelectrochemical CO_2 Reduction with Plasmonic Au/p-GaN Photocathodes. *Nano Lett.* **2018**, *18*, 2545−2550.
(32) Govorov, A. O.; Zhang, W.; Skeini, T.; Richardson, H.; Lee, J.; Kotov, N. A. Gold Nanoparticle Ensembles as Heaters and Actuators: Melting and Collective Plasmon Resonances. *Nanoscale Res. Lett.* **2006**, *1*, 84−90.
(33) Brongersma, M. L.; Halas, N. J.; Nordlander, P. Plasmon-Induced Hot Carrier Science and Technology. *Nat. Nanotechnol.* **2015**, *10*, 25−34.
(34) Jermyn, A. S.; Tagliabue, G.; Atwater, H. A.; Goddard, W. A., III; Narang, P.; Sundararaman, R. Transport of Hot Carriers in Plasmonic Nanostructures. *Phys. Rev. Mater.* **2019**, *3*, 075201.
(35) Zhou, L.; Swearer, D. F.; Zhang, C.; Robatjazi, H.; Zhao, H.; Henderson, L.; Dong, L.; Christopher, P.; Carter, E. A.; Nordlander, P.; Halas, N. J. Quantifying Hot Carrier and Thermal Contributions in Plasmonic Photocatalysis. *Science* **2018**, *362*, 69−72.
(36) Zhang, X.; Li, X.; Reish, M. E.; Zhang, D.; Su, N. Q.; Gutiérrez, Y.; Moreno, F.; Yang, W.; Everitt, H. O.; Liu, J. Plasmon-Enhanced Catalysis: Distinguishing Thermal and Nonthermal Effects. *Nano Lett.* **2018**, *18*, 1714−1723.
(37) Li, X.; Zhang, X.; Everitt, H. O.; Liu, J. Light-Induced Thermal Gradients in Ruthenium Catalysts Significantly Enhance Ammonia Production. *Nano Lett.* **2019**, *19*, 1706−1711.
(38) Naldoni, A.; Guler, U.; Wang, Z.; Marelli, M.; Malara, F.; Meng, X.; Besteiro, L. V.; Govorov, A. O.; Kildishev, A. V.; Boltasseva, A.; Shalaev, V. M. Broadband Hot-Electron Collection for Solar Water Splitting with Plasmonic Titanium Nitride. *Adv. Opt. Mater.* **2017**, *5*, 1601031.
(39) Li, W.; Guler, U.; Kinsey, N.; Naik, G. V.; Boltasseva, A.; Guan, J.; Shalaev, V. M.; Kildishev, A. V. Refractory Plasmonics with Titanium Nitride: Broadband Metamaterial Absorber. *Adv. Mater.* **2014**, *26*, 7959−7965.
(40) Shinde, S. L.; Ishii, S.; Dao, T. D.; Sugavaneshwar, R. P.; Takei, T.; Nanda, K. K.; Nagao, T. Enhanced Solar Light Absorption and Photoelectrochemical Conversion Using TiN Nanoparticle-Incorporated C_3N_4−C Dot Sheets. *ACS Appl. Mater. Interfaces* **2018**, *10*, 2460−2468.
(41) Boltasseva, A.; Shalaev, V. M. All that Glitters Need not be Gold. *Science* **2015**, *347*, 1308−1310.
(42) Barragan, A. A.; Hanukovich, S.; Bozhilov, K.; Yamijala, S. S. R. K. C.; Wong, B. M.; Christopher, P.; Mangolini, L. Photochemistry of Plasmonic Titanium Nitride Nanocrystals. *J. Phys. Chem. C* **2019**, *123*, 21796−21804.
(43) Kreibig, U.; Vollmer, M. *Optical Properties of Metal Clusters*; Springer-Verlag Berlin Heidelberg, 1995; pp. 41−53.
(44) Li, K.; Hogan, N. J.; Kale, M. J.; Halas, N. J.; Nordlander, P.; Christopher, P. Balancing Near-Field Enhancement, Absorption, and Scattering for Effective Antenna−Reactor Plasmonic Photocatalysis. *Nano Lett.* **2017**, *17*, 3710−3717.
(45) Aslam, U.; Chavez, S.; Linic, S. Controlling Energy Flow in Multimetallic Nanostructures for Plasmonic Catalysis. *Nat. Nanotechnol.* **2017**, *12*, 1000−1005.
(46) Chavez, S.; Aslam, U.; Linic, S. Design Principles for Directing Energy and Energetic Charge Flow in Multicomponent Plasmonic Nanostructures. *ACS Energy Lett.* **2018**, *3*, 1590−1596.
(47) Kale, M. J.; Avanesian, T.; Xin, H.; Yan, J.; Christopher, P. Controlling Catalytic Selectivity on Metal Nanoparticles by Direct Photoexcitation of Adsorbate−Metal Bonds. *Nano Lett.* **2014**, *14*, 5405−5412.
(48) Jain, P. K. Taking the Heat off of Plasmonic Chemistry. *J. Phys. Chem. C* **2019**, *123*, 24347−24351.
(49) Dubi, Y.; Sivan, Y. "Hot" Electrons in Metallic Nanostructures-Non-Thermal Carriers or Heating? *Light: Sci. Appl.* **2019**, *8*, 89.
(50) Pavliuk, M. V.; Fernandes, A. B.; Abdellah, M.; Fernandes, D. L. A.; Machado, C. O.; Rocha, I.; Hattori, Y.; Paun, C.; Bastos, E. L.; Sá, J. Nano-Hybrid Plasmonic Photocatalyst for Hydrogen Production at 20% Efficiency. *Sci. Rep.* **2017**, *7*, 8670.
(51) Sugano, Y.; Shiraishi, Y.; Tsukamoto, D.; Ichikawa, S.; Tanaka, S.; Hirai, T. Supported Au-Cu Bimetallic Alloy Nanoparticles: An Aerobic Oxidation Catalyst with Regenerable Activity by Visible-Light Irradiation. *Angew. Chem., Int. Ed.* **2013**, *52*, 5295−5299.
(52) Kim, Y.; Smith, J. G.; Jain, P. K. Harvesting Multiple Electron−Hole Pairs Generated Through Plasmonic Excitation of Au Nanoparticles. *Nat. Chem.* **2018**, *10*, 763−769.
(53) Govorov, A. O.; Richardson, H. H. Generating Heat with Metal Nanoparticles. *Nano Today* **2007**, *2*, 30−38.
(54) Khosravi Khorashad, L.; Besteiro, L. V.; Wang, Z.; Valentine, J.; Govorov, A. O. Localization of Excess Temperature Using Plasmonic Hot Spots in Metal Nanostructures: Combining Nano-Optical Antennas with the Fano Effect. *J. Phys. Chem. C* **2016**, *120*, 13215−13226.